Results in Engineering 29 (2026) 109158

Contents lists available at ScienceDirect

Results in Engineering

journal homepage: www.sciencedirect.com/journal/results-in-engineering

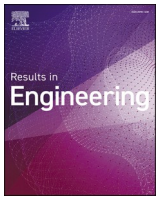

Enhancing the magnetic and electrochemical properties of Cerium-substituted CaMo MOFs through controlled metal nitrates ratios

P Arularasan [a], Mohd Arif Dar [b,h,*], Madhushree Jayaraman [a], P Rajesh [c], S Bala Abirami [d], Bashayr Alanazi [e], Lamiaa Galal Amin [f], Hilal Ahmad Rather [g,*]

[a] Department of Physics, Dwaraka Doss Goverdhan Doss Vaishnav College, Chennai, Tamil Nadu 600106, India
[b] Institute of Power Engineering, Universiti Tenaga Nasional, Jalan IKRAM-UNITEN, Kajang, Selangor-43000, Malaysia
[c] Department of Physics, School of Basic Science, Vels Institute of Science and Technology & Advanced Studies, Pallavaram, Chennai, Tamil Nadu 600117, India
[d] Department of condensed matter physics, Saveetha School of Engineering, Saveetha Institute of Medical and Technical Sciences (SIMATS), Chennai-602105 Tamil Nadu, India
[e] Department of Physics, College of Science, Northern Border University, Arar 73213, Saudi Arabia
[f] Nano-Materials Science Center, Assiut University, Assiut, 71516, Egypt
[g] Department of Biochemistry, Faculty of Biomedical Sciences, Kampala International University, Kampala, Uganda
[h] Faculty of Allied Health Sciences, Chettinad Hospital, and Research Institute, Chettinad Academy of Research and Education, Kelambakkam-603103 Tamil Nadu, India

ARTICLE INFO

Keywords:
Precipitation method
Ferromagnetic materials
Pseudocapacitive nature

ABSTRACT

In this work, Ce-substituted CaMo metal–organic frameworks (MOFs) were successfully synthesized via the precipitation method. The characterization of the synthesized MOFs was performed using various experimental techniques. The XRD confirmed a tetragonal structure, with crystallite sizes ranging from 37 to 49 nm. The XPS shows that the elements Ca, Mo, and Ce are present within the synthesized MOFs. The FTIR shows a slight shift of the peak at 430 cm, indicating Ce incorporation induces structural distortion. The SEM shows well-determined spherical morphology, and EDX confirms an increase in the Ce peak with variation in Ca. The magnetization behaviour of Ce-substituted CaMo MOFs shows their tendency towards soft ferromagnetic materials. The well-defined oxidation/reduction peaks of Ce-substituted CaMo MOFs define their pseudocapacitive nature and tend towards supercapacitor applications.

1. Introduction

MOFs represent one of the fastest-growing classes of materials in modern material science due to their exceptional tunability in porosity, structure, and chemical functionality, arising from their modular assembly of metal ions or clusters with organic linkers [1,2]. This modular nature enables the rational design of diverse framework architectures tailored for a wide range of applications, including gas storage, separation, catalysis, luminescence, magnetism, and energy storage [1–3]. Among the various MOF families, transition-metal-based MOFs have demonstrated remarkable multifunctionality beyond conventional adsorption-based applications, owing to their diverse coordination environments and redox-active metal centres [1,3]. In particular, molybdenum-based MOFs have gained increasing attention due to the multiple accessible oxidation states of Mo and the formation of highly stable frameworks through strong Mo-O bonding [4,5]. The incorporation of alkaline-earth metals such as calcium further improves framework robustness and chemical stability, yielding materials that combine mechanical durability with functional adaptability [5,6].

The introduction of rare-earth elements, especially cerium, as dopants has emerged as an effective strategy to tune the electronic, magnetic, and electrochemical properties of MOFs and MOF-derived materials [7–9]. Cerium exhibits mixed valence states (Ce^{3+}/Ce^{4+}) and strong 4f electronic interactions, which significantly influence charge-transfer processes, defect chemistry, and magnetic exchange interactions [7,8]. Ce-based MOFs have been shown to exhibit multifunctional behaviour, including catalytic and enzyme-mimetic activity, highlighting the versatility of Ce-centred frameworks [9]. In addition, Ce substitution in inorganic and hybrid systems has been reported to induce room-temperature ferromagnetism, demonstrating its ability to manipulate spin-dependent properties through exchange coupling mechanisms [10]. Despite these promising attributes, systematic

* Corresponding authors.
E-mail addresses: dararifphy@gmail.com (M.A. Dar), hilal@kiu.ac.ug (H.A. Rather).

https://doi.org/10.1016/j.rineng.2026.109158
Received 4 November 2025; Received in revised form 29 December 2025; Accepted 15 January 2026
Available online 16 January 2026

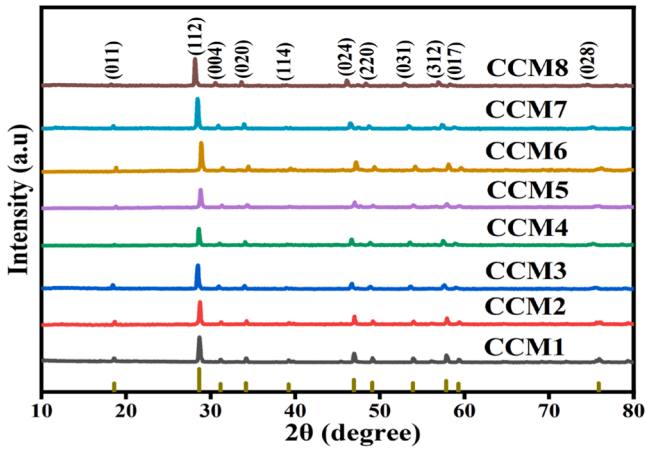

Fig. 1. XRD pattern of the CCM1, CCM2, CCM3, CCM4, CCM5, CCM6, CCM7 and CCM8 MOFs, respectively.

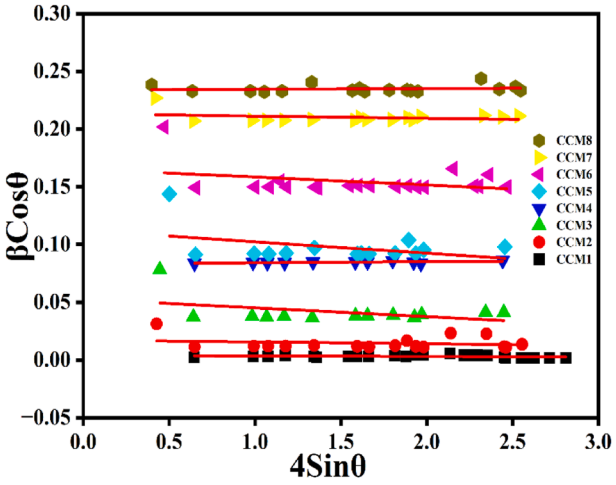

Fig. 2. WH plot of the CCM1, CCM2, CCM3, CCM4, CCM5, CCM6, CCM7 and CCM8 MOFs, respectively.

investigations focusing on Ce incorporation into CaMo-based MOFs and its influence on structural property relationships remain rare [11,12].

Magnetic properties in transition metals and rare-earth-modified MOFs are of significant interest because they provide an ideal platform for studying spin-lattice interactions, exchange coupling, and electron delocalization within highly tunable crystalline frameworks [8,13]. Unlike conventional oxides or metallic alloys, MOFs offer precise control over coordination geometry and metal–metal separation, enabling the deliberate engineering of long-range magnetic ordering through controlled cation substitution [11,14]. Furthermore, the coexistence of variable oxidation states such as Ce^{3+}/Ce^{4+} and Mo^{5+}/Mo^{6+} facilitates mixed-valence interactions, which strongly affect spin alignment, magnetic ordering, and electronic transport behaviour [4,8]. MOF-derived hybrid materials with redox-active metal centres have demonstrated enhanced electrochemical performance, underscoring the close relationship between charge-storage mechanisms and electronic structure [15]. Establishing correlations between magnetic and electrochemical properties is therefore crucial for the development of advanced multifunctional materials in which spin-dependent phenomena and charge storage are intrinsically coupled, enabling applications in spintronics, magnetic sensors, and hybrid energy-storage devices [10–16].

In the present work, we report the synthesis of a new series of eight different Ce-substituted CaMo MOFs, denoted as CCM1, CCM2, CCM3, CCM4, CCM5, CCM6, CCM7 and CCM8, which were synthesized with varying Ce/Ca/Mo ratios according to the general formula $Ce_xCa_{1-x}Mo_y$ for CCM1-CCM4 and $Ce_yCa_xMo_{1-y}$ for CCM5 to CCM8 MOFs. In this notation, x and y represent the molar fraction of Ce^{3+} substituting the Ca^{2+} or Mo^{6+} sites. Specifically, CCM1-CCM4 are Ca-site-dominated compositions with $x = 0.01 - 0.04$ (1–4 mol % Ce^{3+}) and full Mo content ($y = 1$), while CCM5-CCM8 are Mo-site–dominated compositions with $y = 0.01 - 0.04$ (1–4 mol % Ce^{3+}) and full Ca content ($y = 1$). The exact precursor concentrations for each sample are summarized in Table S1. The phase purity, bonding environments, and microstructural features of the CCM1, CCM2, CCM3, CCM4, CCM5, CCM6, CCM7, and CCM8 were established by XRD, FTIR, Raman, SEM/EDAX, and XPS, respectively. In order to investigate their multifunctionality, the magnetic properties of CCM1, CCM2, CCM3, CCM4, CCM5, CCM6, CCM7, and CCM8 MOFs were studied by VSM. Further, the electrodes of CCM1, CCM2, CCM3 and CCM4 MOFs were prepared and used for the CV and EIS studies.

2. Experimental Section

The materials, methods, characterizations, and electrode formation used for the studies are discussed in the supplementary file.

3. Results and discussions

Fig. 1 shows the XRD spectra of the CCM1, CCM2, CCM3, CCM4, CCM5, CCM6, CCM7 and CCM8 MOFs. The XRD peaks are observed at $2\theta = 18.59°$, $28.64°$, $31.16°$, $34.16°$, $39.69°$, $46.93°$, $49.10°$, $53.91°$, $57.82°$, $59.29°$, and $75.86°$, corresponding to (hkl) values (011), (112), (004), (020), (114), (024), (220), (031), (312), (017), and (028), respectively. All these diffraction peaks match well with the tetragonal scheelite $CaMoO_4$ phase without resolvable secondary phases (Reference code: 96-157-0755). The absence of extra reflections further indicates that Ce incorporation, either at the Ca or at the Mo site, does not induce the formation of secondary or impurity phases. For the CCM1, CCM2, CCM3 and CCM4 MOFs, in which Ce^{3+} partly substitutes Ca^{2+}, with Mo remaining constant, the diffraction peaks are still sharp and intense, thus indicating high crystallinity. Only slight broadening and differences in peak intensity are observed, which suggests that the structural strain is minimal. This is further a result of the near-comparable ionic radii for Ca^{2+} (1.00 Å) and Ce^{3+} (1.01 Å), where the equivalent replacement of Ca by Ce allows the latter to be hosted at the A-site with negligible lattice distortion [17,18]. The results confirm that Ce substitution at the Ca-site is structurally beneficial. However, for the CCM5, CCM6, CCM7, and CCM8 MOFs, in which Ce is substituted at the Mo site, with Ca remaining constant, there is a shifting of the peaks indicating changes in lattice parameters due to Ce incorporation. This peak shifting arises from lattice distortion induced by Ce substitution, particularly when Ce occupies the Mo site, where the large ionic radius mismatch and valence difference promote structural deformation and charge-compensation mechanisms such as oxygen vacancy formation. The difference in ionic radii explains the contrasting lattice responses. Doping at the Ca^{2+} site (1.00 Å) with Ce^{3+} (1.01 Å) involves nearly identical ionic sizes, leading to negligible lattice strain. In contrast, substitution of Mo^{6+} (0.62 Å) by the much larger and lower-valence Ce^{3+} causes significant structural distortion and requires charge-compensation mechanisms, most likely through the formation of oxygen vacancies. However, it can be pointed out from the beginning of the CCM1 MOF that two peaks were observed at $46.93°$ and $57.82°$, which do not match those observed in the Ref. code 96-157-0755. These two peak positions are at $47.10°$ and $58.07°$, respectively, very close to the peaks seen in the XRD spectra. The little difference in the peak positions is due to the Ce dopant from the beginning of the reaction. The average crystallite size is calculated using the equation (Debye Scherrer's equation).

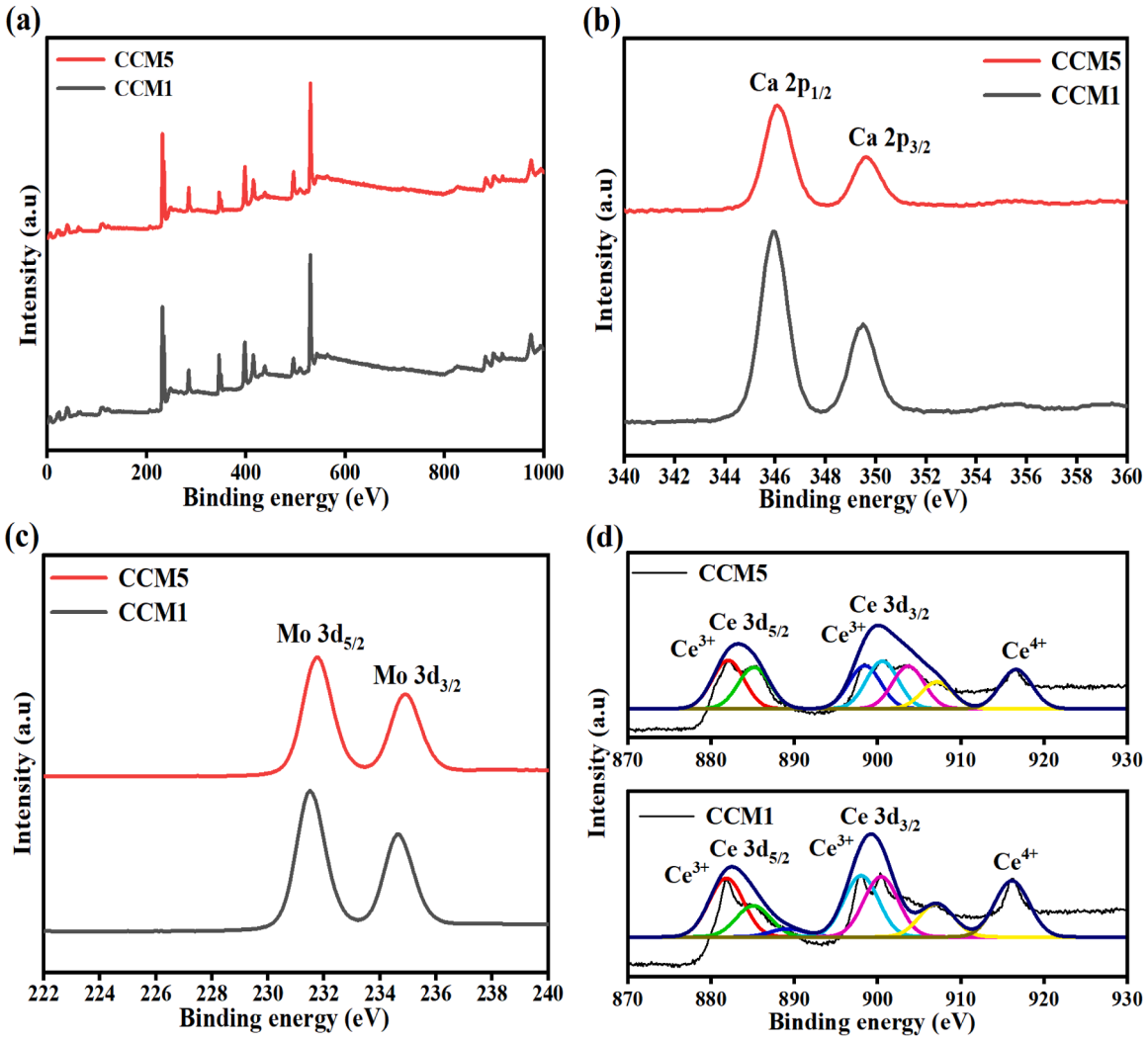

Fig. 3. (a) XPS spectra (b) Ca peaks (c) Mo peaks and (d) Ce peaks of the CCM1 and CCM5 MOFs, respectively.

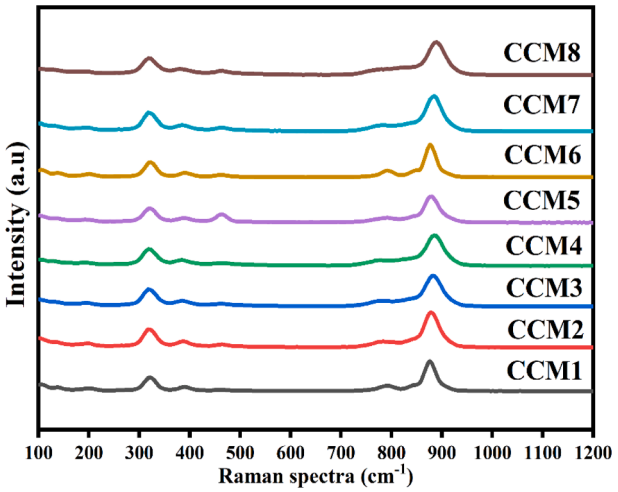

Fig. 4. Raman spectra of the CCM1, CCM2, CCM3, CCM4, CCM5, CCM6, CCM7 and CCM8 MOFs, respectively.

$$D = \frac{n\lambda}{\beta Cos\theta} \quad (1)$$

where symbols have their own meaning. The calculated values are 47, 47, 38, 49, 37, 41, 38, and 39 nm for CCM1, CCM2, CCM3, CCM4, CCM5, CCM6, CCM7, and CCM8 MOFs, respectively. The results indicate that Ce substitution at different incorporation sites has a varying impact on crystallite growth. For the Ca-substitution series of CCM1, CCM2, CCM3, and CCM4 MOFs, the crystallite size remains relatively stable with only slight variations, indicating a minimal lattice distortion due to the closer ionic radii of Ca^{2+} and Ce^{3+}. In contrast, for the Mo-substitution series CCM5, CCM6, CCM7, and CCM8 MOFs, more pronounced variations in crystallite sizes are observed, which could be attributed to the ionic radius and charge incompatibility between Ce^{3+} and Mo^{6+}, followed by the local lattice strain and partial inhibition of the crystallite growth. Further, the lattice parameters and cell volume of the CCM1, CCM2, CCM3, CCM4, CCM5, CCM6, CCM7, and CCM8 MOFs are given in the supplementary file (Table S2).

To gain further insight into the Ce incorporation-induced lattice distortions, the Williamson-Hall (W-H) method was employed (Fig. 2). In contrast to the Scherrer approach, which assumes peak broadening arises exclusively from crystallite size, the W-H analysis separates the contributions from size and microstrain. A plot of βcosθ versus 4sinθ was constructed for each sample, and the linear fitting parameters were used to extract the stress (σ) using the relation:

$$\sigma = \varepsilon E \quad (2)$$

where ε is the strain obtained from the slope of the W-H plot and E is the

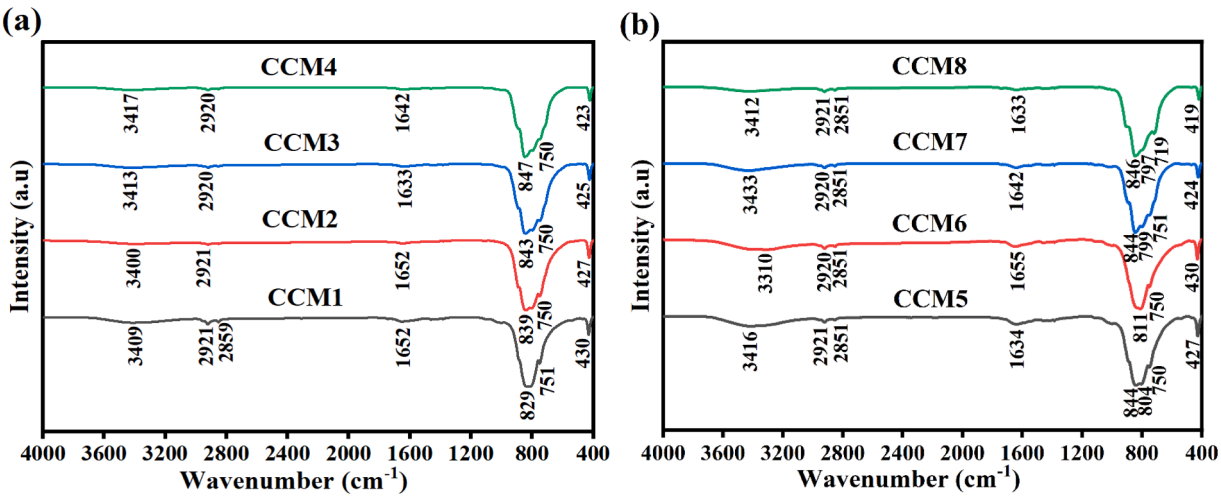

Fig. 5. (a, b) FTIR spectra of the CCM1, CCM2, CCM3, CCM4, CCM5, CCM6, CCM7 and CCM8 MOFs, respectively.

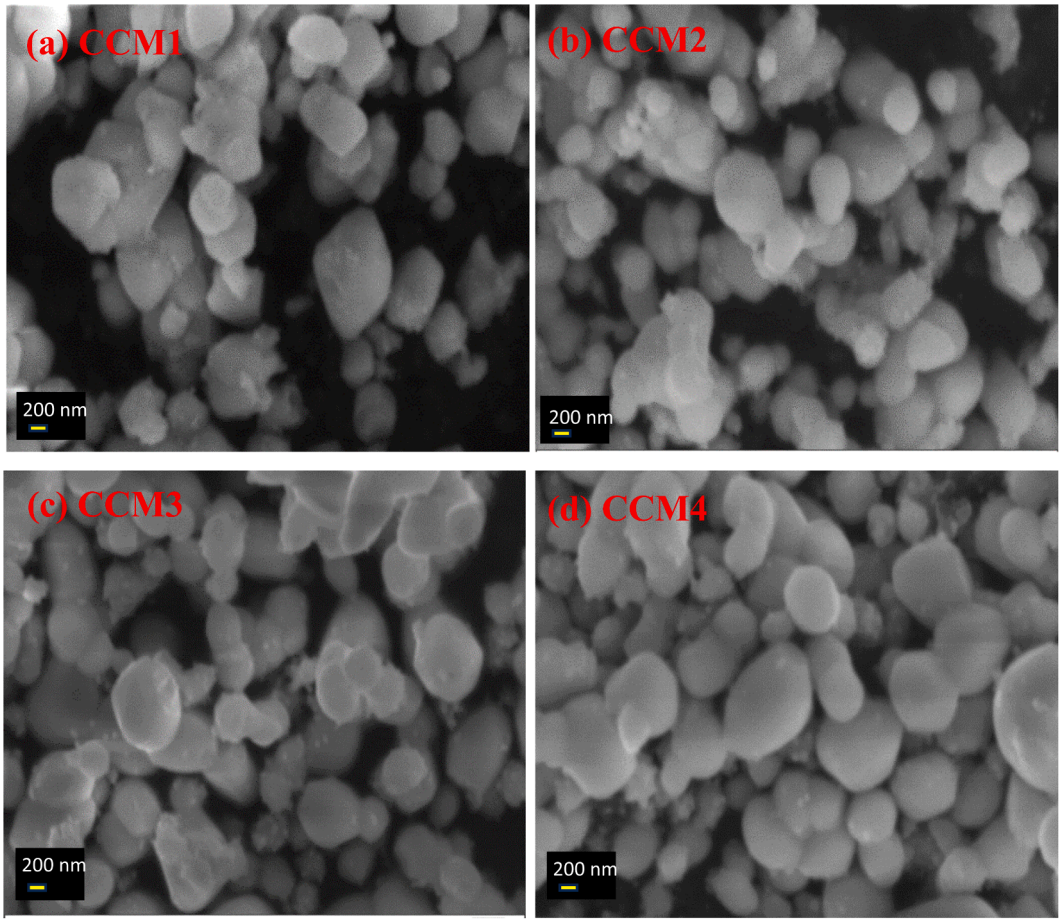

Fig. 6. (a-d) SEM images of the CCM1, CCM2, CCM3 and CCM4 MOFs, respectively.

Young's modulus of the material. The calculated stress values are 0.077, 0.152, 0.351, 0.032, 0.440, 0.350, 0.152 and 0.070 (GPA) for CCM1, CCM2, CCM3, CCM4, CCM5, CCM6, CCM7, and CCM8 MOFs, respectively. These values indicate that Ce doping generates measurable internal stresses within the $CaMoO_4$ lattice. In the case of Ca-site substitution, the values are relatively low due to the similar ionic radii between Ca^{2+} and Ce^{3+}, while for Mo-site substitution, higher values are observed, which may be associated with the significant size and charge difference between Ce^{3+} and Mo^{6+}. Overall, XRD analysis highlights that Ce substitution at a Ca site maintains the structural stability with very little distortion, whereas substitution at the Mo site induces more significant lattice perturbation. The findings point toward the different structural roles of Ca and Mo ions in the stabilization of the scheelite lattice and provide an effective way of tuning crystallographic and microstructural properties of Ce-substituted CaMo MOFs.

To verify the successful incorporation of Ce and Mo into the CaMo framework, XPS analyses were performed. Fig. 3a presents the full survey spectra of CCM1 and CCM5 MOFs, confirming the presence of the

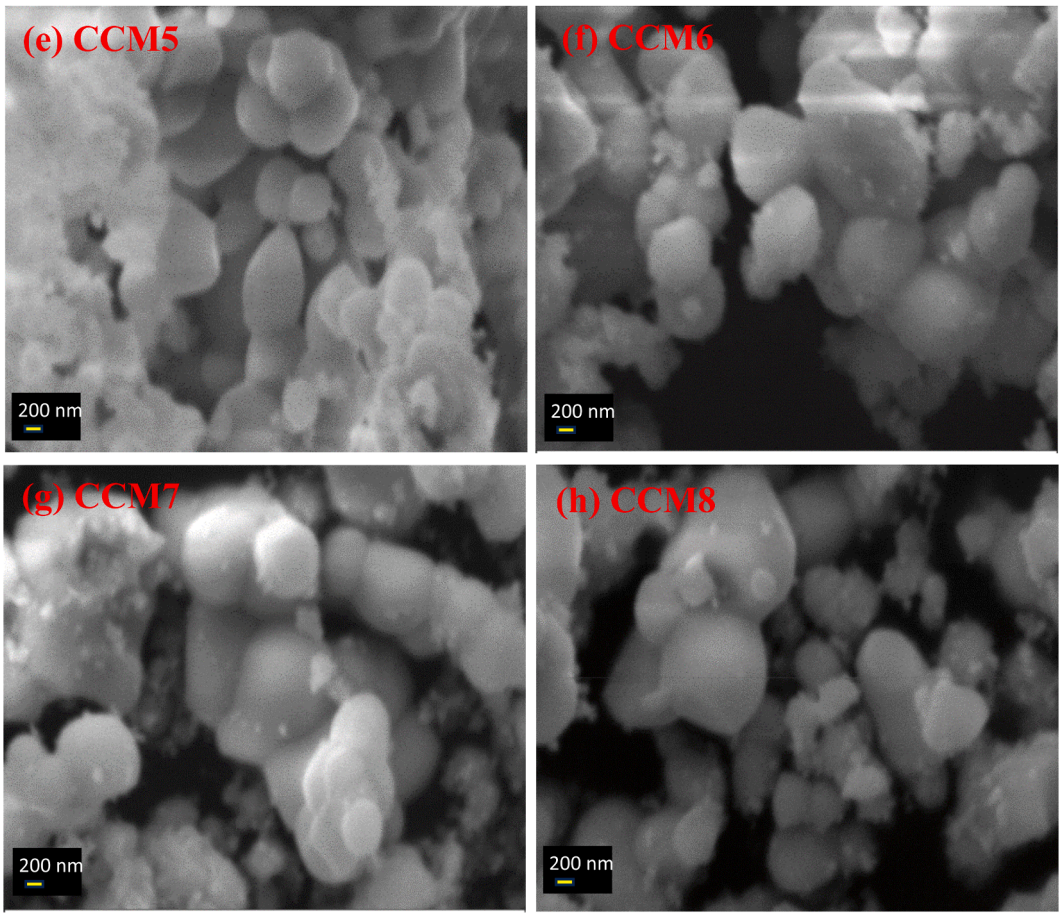

Fig. 6. (e-h) SEM images of the CCM5, CCM6, CCM7 and CCM8 MOFs, respectively.

constituent elements. The high-resolution deconvolution of Ca 2p spectra for CCM1 and CCM5 displays distinct peaks in the range of 344-352 eV, corresponding to Ca $2p_{1/2}$ and Ca $2p_{3/2}$ states (Fig. 3b) [19]. Similarly, the Mo 3d spectra reveal peaks within 228-232 eV, attributed to Mo $3d_{5/2}$ and Mo $3d_{3/2}$ states (Fig. 3c) [20]. The Ce 3d spectra exhibit multiple peaks between 870 and 930 eV, characteristic of both Ce^{3+} and Ce^{4+} oxidation states, confirming the mixed-valence nature of cerium in the structure (Fig. 3d) [21]. The deconvolution curves of the Ca, Mo, and Ce spectra clearly demonstrate the successful incorporation of Ce in all MOF compositions (CCM1-CCM8). The significant variations in peak intensity and broadening between CCM1 and CCM5 MOFs are caused by Ce substitution at the Ca sites in CCM1-CCM4 MOFs and at the Mo sites in CCM5-CCM8 MOFs. Further, the atomic and photoelectron peak percentage of elements are given in Table S3.

Fig. 4 presents the Raman spectra of CCM1, CCM2, CCM3, CCM4, CCM5, CCM6, CCM7 and CCM8 MOFs. The dominant band at ~872 cm^{-1} corresponds to the symmetric stretching vibration (ν1, Ag) of Mo-O bonds in the MoO_4 tetrahedra, while additional modes at ~321 cm^{-1} (Ag), 391 cm^{-1} (Eg), and 787 cm^{-1} (Eg) are assigned to internal vibrations of $(MoO_4)^{2-}$ units [11]. For the CCM1-CCM4 MOFs, wherein Ce replaces Ca, very slight spectral changes are observed, demonstrating some lattice distortions, whereas for the CCM5-CCM8 MOFs with Ce for Mo substitution, more pronounced shifts and band broadening can be seen, especially in ν1, corresponding to a stronger perturbation in the Mo-O tetrahedra. The progressive peak shift in the sequence of CCM1, CCM2, CCM3, CCM4, CCM5, CCM6, CCM7 and CCM8 MOFs confirms the effective incorporation of Ce, with much more pronounced structural modification when Ce substitutes Mo rather than Ca.

Fig. 5 (a,b) illustrates the FTIR spectra of CCM1, CCM2, CCM3, CCM4, CCM5, CCM6, CCM7, and CCM8 MOFs, respectively. All the synthesized MOFs show characteristic vibrational modes representative of the CaMo framework. The absorption at 751 cm^{-1} corresponds to the antisymmetric stretching vibration of the Mo-O bond in the $(MoO_4)^{2-}$ tetrahedra and the band at 430 cm^{-1} is related to Ca-O vibrations [12, 14]. The decrease in intensity and slight shifts of these bands within CCM1, CCM2, CCM3, CCM4, CCM5, CCM6, CCM7, and CCM8 MOFs reflect structural distortions caused by Ce incorporation. Furthermore, the band at 829 cm^{-1} is due to the asymmetric O-Mo-O stretching mode [22]. The absorption peaks at 1652 and 3409 cm^{-1} are due to the bending and stretching vibrations of water molecules, respectively, while the band at 2859 cm^{-1} corresponds to C-H stretching vibrations [5]. All these absorptions collectively indicate the presence of Ca-O and Mo-O linkages as the fundamental building blocks of the framework, with slight changes induced by Ce doping.

The surface morphology of CCM1, CCM2, CCM3, CCM4, CCM5, CCM6, CCM7 and CCM8 MOFs was studied by using SEM and their corresponding images are presented in Fig. 6(a-h). All samples predominantly showed a spherical morphology, confirming the uniform growth of crystallites during synthesis. For the case of CCM1-CCM4 MOFs, in which Ce is incorporated at the Ca site while maintaining the same Mo content, the particles are well-defined and show clearly distinguishable spherical domains that become more homogeneous, with clearly separated domains for higher Ce contents, as depicted in Fig. 6a-d. In fact, this improvement in morphological regularity may be ascribed to the stabilization effect promoted by the substitution of Ce at the Ca site that favors crystallization and diminishes structural imperfections.

In contrast to this, for the CCM5-CCM8 MOFs, where Ce substitutes at the Mo site, significant changes in morphology are observed. The spherical particles appear larger and slightly agglomerated compared to

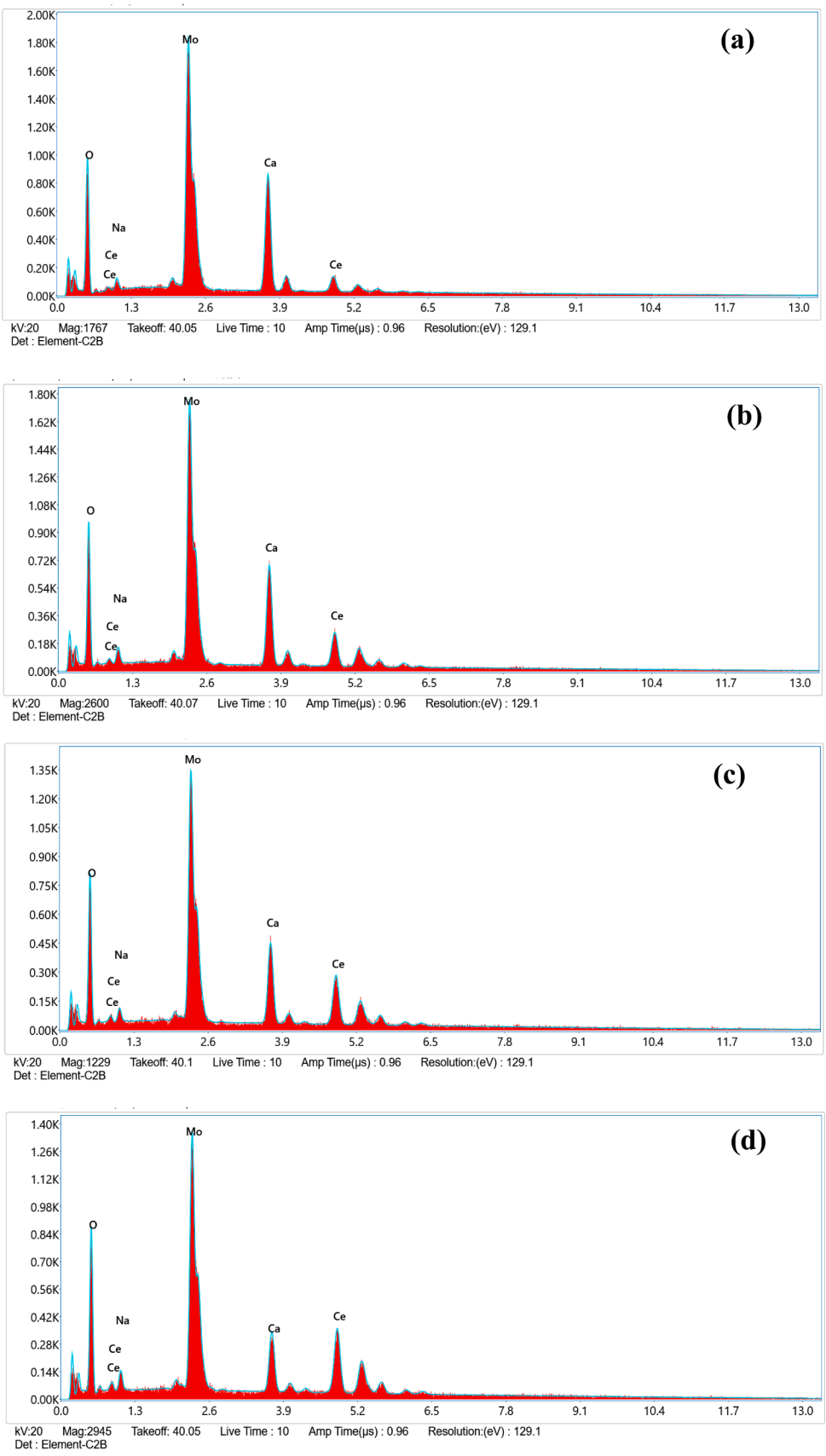

Fig. 7. (a-d) EDX spectra of the CCM1, CCM2, CCM3 and CCM4 MOFs, respectively.

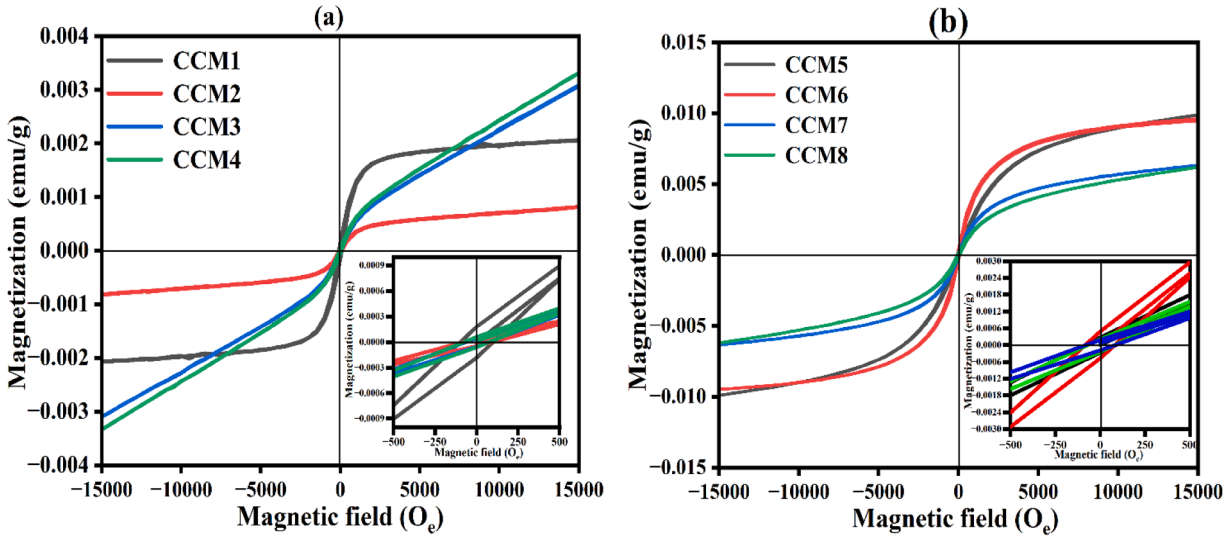

Fig. 8. (a, b) VSM of the CCM1, CCM2, CCM3, CCM4, CCM5, CCM6, CCM7 and CCM8 MOFs, respectively.

Table 1
Magnetic parameters of the CCM1, CCM2, CCM3, CCM4, CCM5, CCM6, CCM7 and CCM8 MOFs.

Samples	Magnetization 'Ms' (emu/g)	Intrinsic coercivity 'Hc' (Oe)	Retentivity 'Mr' (emu)	SQR = Mr/Ms
CCM1	0.00206	97.76	0.000181	0.0878
CCM2	0.00081	87.23	0.000045	0.0555
CCM3	0.00308	68.50	0.000050	0.0162
CCM4	0.00313	74.05	0.000058	0.0185
CCM5	0.00986	86.23	0.000277	0.0280
CCM6	0.00959	82.54	0.000478	0.0498
CCM7	0.00631	75.18	0.000226	0.0358
CCM8	0.00619	80.88	0.000186	0.0300

the CCM1-CCM4 MOFs (Fig. 6e-h). These might be attributed to the substitution of Ce for Mo, which incorporates changes in ionic size and differences in oxidation states (Ce^{3+}/Ce^{4+} versus Mo^{6+}) and thus induces lattice strain and modifies the growth kinetics, facilitating partial coalescence of particles and leading to less regular morphologies. In summary, from SEM analysis, a clear trend is developed between the site of Ce substitution and morphological evolution, i.e., Ce doping at the Ca site promotes spherical uniformity, while substitution at the Mo site induces agglomeration and enlargement of particles. Fig. 7 (a-d) illustrates the EDX spectra of the CCM1, CCM2, CCM3, and CCM4 MOFs, respectively. EDX spectra confirm Ce doping in the CCM1, CCM2, CCM3, and CCM4 MOFs. It can be seen that the concentration of Ce ions increases from CCM1 to CCM4 MOFs, determining their successful incorporation. Also, some content of Na is seen in the EDAX spectra, which might be due to the Sodium Molybdate used during the synthesis of CCM1, CCM2, CCM3, and CCM4 MOFs.

The magnetic behavior of the CCM1, CCM2, CCM3, CCM4, CCM5, CCM6, CCM7 and CCM8 MOFs was examined using vibrating sample magnetometry (VSM) at room temperature to investigate the influence of Ce incorporation on their magnetic properties. The magnetization (M-H) curves were recorded to determine the key magnetic parameters, including saturation magnetization (Ms), remanent magnetization (Mr), and coercivity (Hc). Fig. 8 (a, b) shows the VSM spectra of the CCM1, CCM2, CCM3, CCM4, CCM5, CCM6, CCM7 and CCM8 MOFs. All samples exhibit a typical S-shaped magnetization behavior with no significant hysteresis loop, which is characteristic of paramagnetic or soft ferromagnetic materials. Among the series, CCM5 and CCM6 display the highest magnetization values (0.00986 emu/g and 0.00959 emu/g), indicating enhanced magnetic response compared to the other compositions. The CCM2, on the other hand, shows the lowest magnetization, suggesting a nearly diamagnetic character with negligible response to the applied field. The gradual increase in magnetization from CCM3 to CCM8 reflects the compositional dependence of the magnetic properties, likely originating from variations in the Ce/Ca/Mo ratio and its influence on unpaired electron density. The magnetic parameters of the CCM1, CCM2, CCM3, CCM4, CCM5, CCM6, CCM7 and CCM8 MOFs were systematically analyzed to gain insights into their intrinsic properties (Table 1). The hysteresis curves derived from VSM measurements reveal extremely low coercivity values, ranging from 68.50 Oe in CCM3 to 97.76 Oe in CCM1 MOFs. These values are characteristic of soft magnetic systems, where the energy required to reverse the magnetization is minimal. Such low coercivity suggests weak magnetic domain interactions and a strong tendency toward reversible magnetization under an external field. The Ms values of the synthesized MOFs vary from 8.1×10^{-4} emu/g in CCM2 to 9.8×10^{-3} emu/g in CCM5. Among the series, CCM5 and CCM6 MOFs display the largest magnetization, signifying an enhanced contribution of unpaired electrons or paramagnetic centers within their frameworks. By contrast, CCM2 MOF exhibits the lowest magnetization, indicating a nearly diamagnetic character with very limited field-induced spin alignment. The observed compositional dependence suggests that a slight variation in the Ce/Ca/Mo ratio strongly modulates the density of localized magnetic moments. The values of Mr further establish the weak magnetic behavior of these materials. The recorded values remain within the range of 4.5×10^{-5} to 4.78×10^{-4} emu, which is significantly lower than those generally reported for conventional ferromagnetic nanostructures. Among all the synthesized MOFs, CCM6 MOF shows the highest remanent magnetization, implying a relatively stronger spin alignment that is not entirely lost after the removal of the external field. In contrast, CCM2 MOF exhibits the lowest remanence, indicating its limited ability to retain magnetization. The squareness ratio given by ($SQR = Mr/Ms$) provides additional insights into the nature of the magnetic ordering. The calculated SQR values fall between 0.0162 and 0.0878, which is well below the threshold of 0.5 that typically distinguishes single-domain ferromagnetic materials. The consistently low SQR values confirm the superparamagnetic-like or weakly paramagnetic nature of the MOFs. Among the series, CCM1 MOF exhibits the highest SQR (0.0878), suggesting a relatively greater proportion of aligned magnetic moments retained after field removal. Conversely, CCM3 and CCM4 MOFs display the lowest SQR values, indicating negligible magnetic ordering and nearly complete reversibility of magnetization. The combined

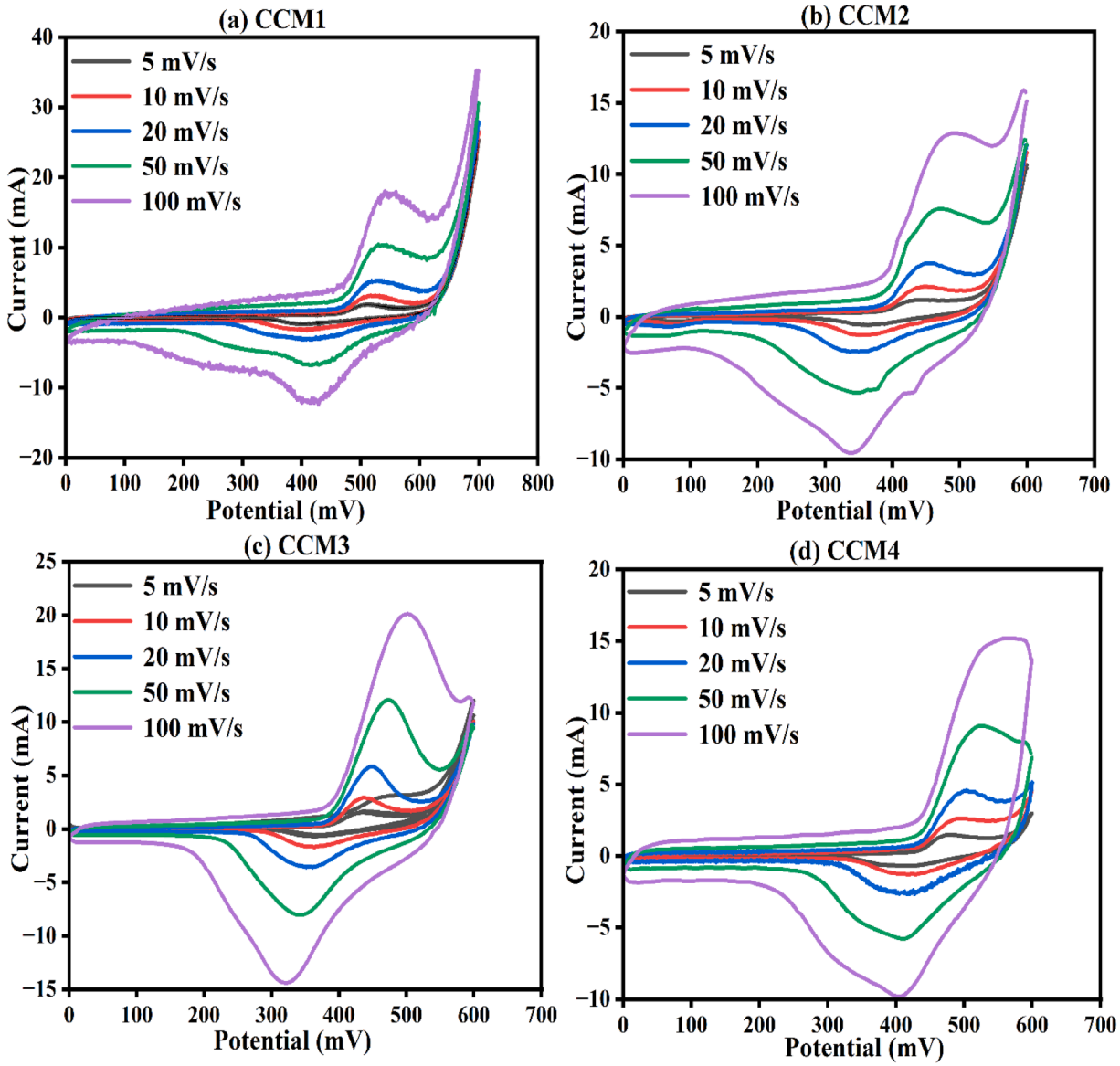

Fig. 9. (a-d) CV curves of the CCM1, CCM2, CCM3 and CCM4 electrodes, respectively.

coercivity, magnetization, retentivity, and SQR indicate that the CCM1, CCM2, CCM3, CCM4, CCM5, CCM6, CCM7, and CCM8 MOFs behave predominantly as soft magnetic systems.

The CV studies of the CCM1, CCM2, CCM3, and CCM4 electrodes were recorded at various scan rates ranging from 5 to 100 mV/s (Fig. 9 a-d). At lower scan rates, the curves of CCM1, CCM2, CCM3, and CCM4 electrodes look more defined in shape because electrolyte ions have enough time to diffuse inside the framework and reach the redox-active sites. The current response increases continuously as the scan rate increases, showing that the current is exactly proportional to the scan rate. However, curve distortion and widening also represent the kinetic limitation and resistance effect present in the electrode material. The consistent rise in current with potential at a greater scan rate of CCM1, CCM2, CCM3, and CCM4 electrodes suggests an increased capacitive contribution of a pseudocapacitive nature [13]. Furthermore, the increase in the enclosed area of the CV curves with the scan rate evidently demonstrates the hybrid storage mechanism, which combines both electric double-layer capacitance and faradaic charge transfer. Fig. 10 (a) shows the peak-to-peak separation of the CCM1, CCM2, CCM3 and CCM4 electrodes, respectively. Here, it is observed that both the anodic and cathodic peak currents increase linearly with the scan rate. However, the electrochemical storage mechanism of the CCM1, CCM2, CCM3 and CCM4 electrodes was usually demonstrated through a power law given as

$$i = av^b \tag{3}$$

$$\log(i_p) = \mathrm{Loga} + \mathrm{blogv} \tag{4}$$

Here, a and b are constants, i is the current and v is the scan rate (mV/s). The b values are estimated by plotting log (v) versus log (i). Fig. 10 (b) illustrates the power-law relationship of the CCM1, CCM2, CCM3 and CCM4 electrodes, respectively. The validity of this model for CCM1, CCM2, CCM3, and CCM4 electrodes is shown by the linear fits of log i vs log v with strong correlation coefficients (R^2 = 0.997-0.999). In contrast to strictly diffusion-controlled processes, the retrieved b values for CCM1 (0.715), CCM2 (0.805), CCM3 (0.852), and CCM4 (0.746) electrodes fall between 0.5 and 1.0, suggesting a mixed charge-storage behavior dominated by pseudocapacitive contributions. In comparison to the other compositions, CCM3 has the greatest b value, indicating quicker surface-controlled kinetics and better electrochemical activity.

Furthermore, the Trasatti method was applied to quantify the surface-controlled and diffusion-controlled charge storage contributions

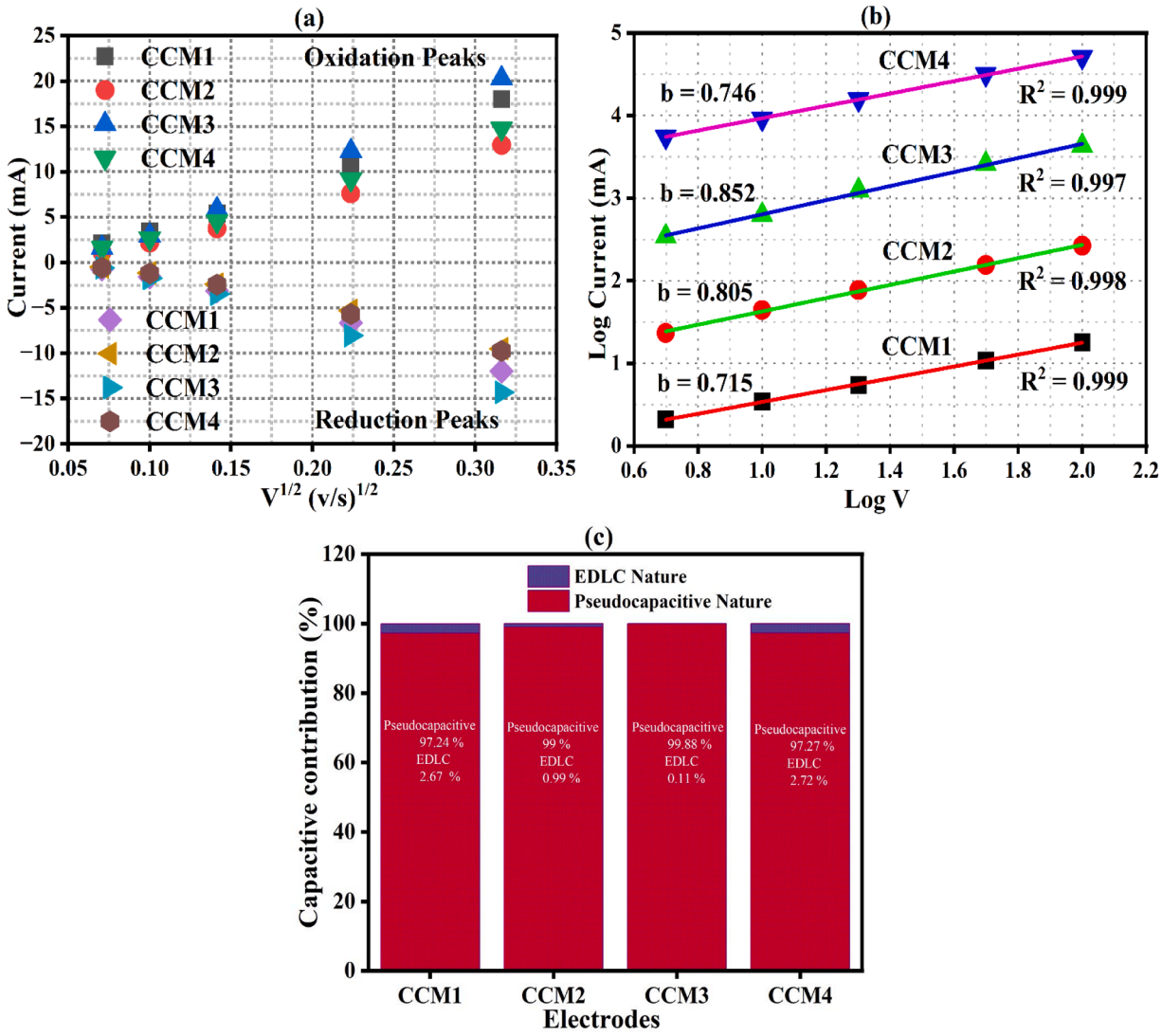

Fig. 10. (a) peak to peak separation (b) Log V versus Log current and (c) electrodes versus capacitive contribution of the CCM1, CCM2, CCM3 and CCM4 electrodes, respectively.

of the CCM1, CCM2, CCM3, and CCM4 electrodes. Based on the Equation $C_i = C_T - C_o$, the total specific capacitance (C_T), surface-controlled capacitance (C_o), and diffusion-controlled contribution (C_i) of the CCM1, CCM2, CCM3, and CCM4 electrodes were quantitatively evaluated from the linear fitting of the data shown in Fig. 11 (a,b). The extracted capacitance values are summarized in Table 2, while the corresponding percentage contributions arising from diffusion-controlled processes are illustrated in Fig. 10c. The capacitive contribution analysis reveals that charge storage in all CCM1, CCM2, CCM3 and CCM4 electrodes is predominantly governed by pseudocapacitive mechanisms, with a negligible contribution from EDLC. The CCM1 electrode shows a pseudocapacitive fraction of 97.24% (EDLC: 2.67%), which increases further for CCM2 and CCM3 to 99.0% and 99.88%, respectively, indicating a progressive enhancement of rapid surface and near-surface faradaic reactions enabled by improved electroactive sites and ion-transport kinetics. Among all the electrodes, the CCM3 electrode exhibits the highest pseudocapacitive dominance, suggesting an optimal synergy between redox-active centers and ion diffusion. In contrast, CCM4 displays a slight decline in pseudocapacitive contribution (97.27%) with a corresponding increase in EDLC behavior (2.72%), possibly due to limited accessibility of active sites arising from microstructural effects. Overall, these results confirm that the CCM1, CCM2, CCM3 and CCM4 electrodes store charge mainly through fast pseudocapacitive processes, underscoring the effectiveness of compositional and structural optimization in enhancing faradaic charge storage

The specific capacitance values of the CCM1, CCM2, CCM3 and CCM4 electrodes are determined by using the formula

$$Cp = \frac{A}{mSV} \tag{5}$$

Where A is the area of the CV curve, m is the active mass of the material (grams), S is the scan rate (V/s) and V is the potential window (volts). Fig. 12 shows the specific capacitance versus scan rate of the CCM1, CCM2, CCM3 and CCM4 electrodes, respectively. The specific capacitance values are 33, 33, 32, 28, and 25 (F/g) for the CCM1 electrode, 32, 31, 31, 29, and 27 (F/g) for the CCM2 electrode, 34, 33, 32, 32, and 32 (F/g) for the CCM3 electrode and 33, 33, 32, 28, and 25 (F/g) for the CCM4 electrode. The higher specific capacitance values of the CCM3 electrode indicate that a dominant surface-controlled charge storage mechanism occurs, where fast and reversible redox reactions occur at the electrode-electrolyte interface. Overall, the variations found in the specific capacitance of the CCM1, CCM2, CCM3, and CCM4 electrodes can be related to differences in surface morphology, accessibility to active sites, and charge transfer dynamics. The relatively stable capacitance of the CCM3 electrode at higher scan rates indicates its superior rate capability and faster electrochemical kinetics. While the

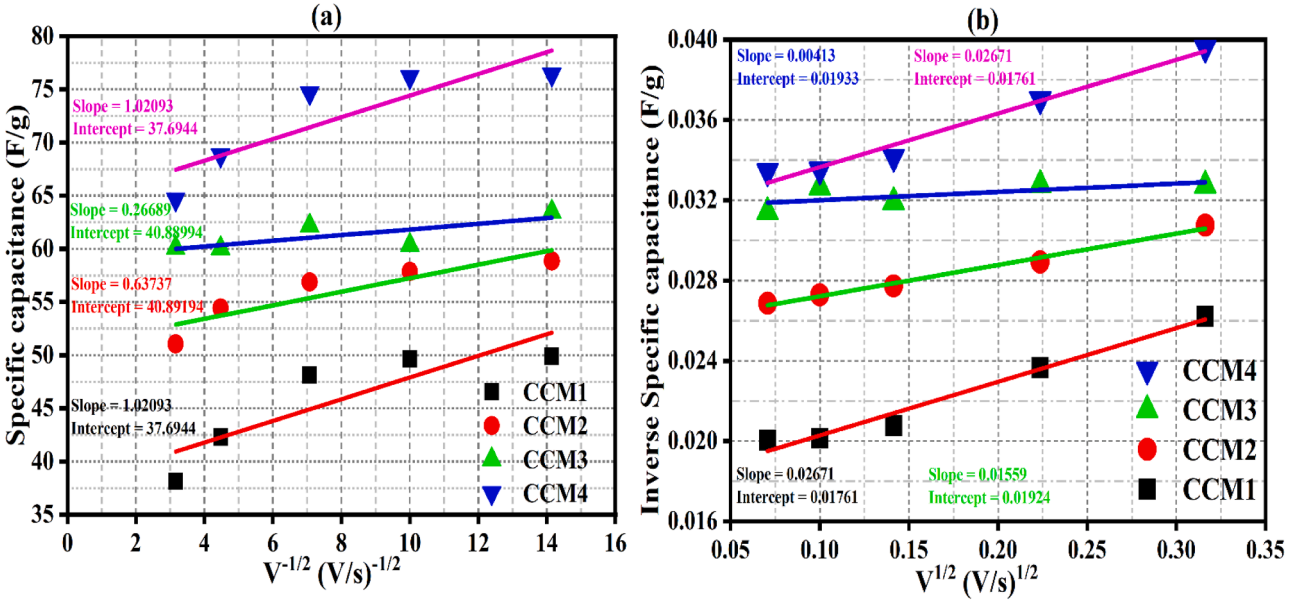

Fig. 11. (a) Inverse square root of scan rate versus specific capacitance and (b) square root of scan rate versus inverse specific capacitance of the CCM1, CCM2, CCM3 and CCM4 electrodes, respectively.

Table 2
C_i, C_T and C_o values of the CC1, CCM2, CCM3 and CCM4 electrodes.

Sample	C_T	C_o	C_i
CCM1	37.43	1.02093	36.40
CCM2	64.14	0.63737	63.50
CCM3	242.13	0.26689	241.86
CCM4	37.43	1.02093	36.41

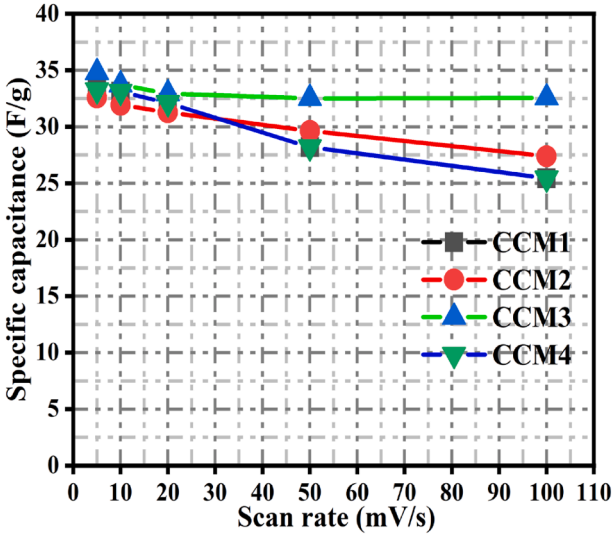

Fig. 12. Specific capacitance versus scan rate of the CCM1, CCM2, CCM3 and CCM4 electrodes, respectively.

stable performance of CCM1 and CCM2 may suggest enhanced reversibility and favorable ion diffusion characteristics, making them potential candidates for efficient energy storage. A comparative study of specific capacitance values with the literature report is given in Table 3.

To further elucidate the electrochemical conductivity and interfacial charge-transfer behavior of the CCM1, CCM2, CCM3, and CCM4 electrodes, electrochemical impedance spectroscopy (EIS) measurements

Table 3
Comparative study of specific capacitance values of the present work with the literature report.

S. No	Electrode Material	Electrolyte	Specific Capacitance	Ref.
1.	Mo-doped LDHs@MOF-Se	KOH	5.16 C cm^{-2}	23
2.	$CoSe_2$/CNT	KOH	58.4 $mAhg^{-1}$	24
3.	MnSe@NF	KOH	62.4 $mAhg^{-1}$	25
4.	Mo-doped LDHs@MOF-Se	KOH	132 Fg^{-1}	23
5.	CC@@CoO@S-Co_3O_4	PVA/KOH	1.99 Fcm^{-1}	26
6.	$CuCo_2S_4$ NS	PVA/KOH	~ 2.1 $mAhcm^{-3}$	27
7.	M-MOF-74	KCl	0.05-1.94 F/g	28
8.	Co-L/MOF	KOH	74 Fg^{-1}	29
9.	CCM3	KOH	34 F/g	Present work

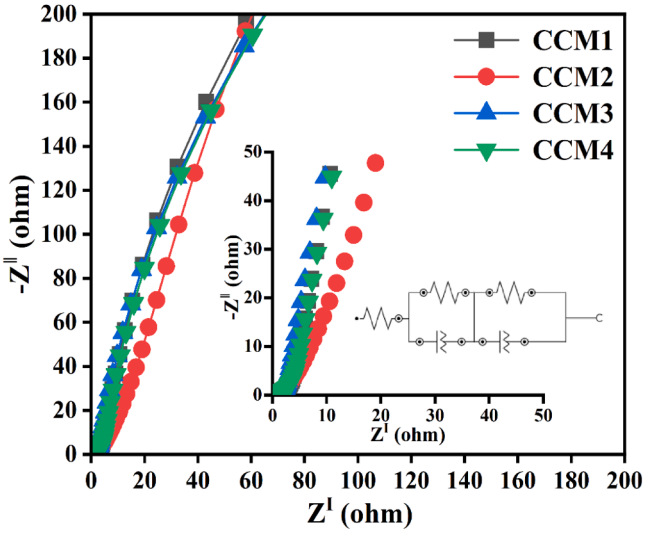

Fig. 13. Nyquist plot of the CCM1, CCM2, CCM3 and CCM4 electrodes, respectively.

were carried out. Fig. 13 presents the corresponding Nyquist plots of the CCM1, CCM2, CCM3 and CCM4 electrodes, respectively. All samples exhibit typical capacitive characteristics, with the absence of a well-defined semicircular feature in the high-frequency region and the presence of an inclined line in the low-frequency region. This behavior suggests that the electrochemical processes are predominantly governed by ion diffusion and capacitive charge storage rather than being limited by charge-transfer resistance. The extracted series resistance (R_s) values for CCM1, CCM2, CCM3, and CCM4 electrodes are 1.00, 0.90, 1.10, and 0.85 (Ω), respectively, indicating low internal resistance and good electrical conductivity of the electrode materials. The corresponding charge-transfer resistance (R_{ct}) values are 1.80, 2.30, 2.70, and 2.55 (Ω), respectively, reflecting efficient interfacial charge-transfer kinetics, with CCM1 exhibiting the lowest Rct and thus the most favorable electron-transfer behaviour. Overall, the low Rs and moderate Rct values collectively confirm efficient charge transport and rapid electrochemical kinetics, which are consistent with the superior capacitive performance of the CCM1, CCM2, CCM3 and CCM4 electrodes.

4. Conclusion

Ce-substituted CaMo-based MOFs were synthesized through a simple precipitation route and systematically characterized to illustrate their structural, morphological, magnetic, and electrochemical properties. The XRD confirmed the formation of a tetragonal phase with nanoscale crystallite sizes, and XPS and EDX confirmed the presence of Ce within the CaMo framework. These Ce substitutions result in slight structural distortions, as reflected in the observed FTIR peak shifts. The SEM images revealed spherical morphologies with uniform sizes. The Magnetic studies indicated soft ferromagnetic behavior in the synthesized MOFs. The well-defined redox peaks in the respective CV curves indicate the pseudocapacitive nature of the electrodes. Overall, Ce-substituted CaMo MOFs are promising due to their structural stability, magnetic tunability, and corresponding electrochemical activity.

CRediT authorship contribution statement

P Arularasan: Writing – original draft, Resources, Methodology, Formal analysis, Data curation, Conceptualization. **Mohd Arif Dar:** Writing – original draft, Visualization, Software, Methodology, Formal analysis, Data curation, Conceptualization. **Madhushree Jayaraman:** Writing – review & editing, Formal analysis, Conceptualization. **P Rajesh:** Resources. **S Bala Abirami:** Resources. **Bashayr Alanazi:** Resources, Funding acquisition. **Lamiaa Galal Amin:** Resources. **Hilal Ahmad Rather:** Resources, Methodology, Investigation, Formal analysis, Data curation, Conceptualization.

Declaration of competing interest

The authors declare that they have no known competing financial interests or personal relationships that could have appeared to influence the work reported in this paper.

Acknowledgement

“The authors extend their appreciation to the Deanship of Scientific Research at Northern Border University, Arar, KSA for funding this research work through the project number NBU-FFR-2025- 2601-03”.

Supplementary materials

Supplementary material associated with this article can be found, in the online version, at doi:10.1016/j.rineng.2026.109158.

Data availability

The data that has been used is confidential and is available to the corresponding author upon a reasonable request.

References

[1] H. Furukawa, K.E. Cordova, M. O'Keeffe, O.M. Yaghi, The chemistry and applications of metal–organic frameworks, Science 341 (2013) 1230444, https://doi.org/10.1126/science.1230444.
[2] J.L.C. Rowsell, O.M. Yaghi, Metal–organic frameworks: A new class of porous materials, Microporous. Mesopor. Mater. 73 (1–2) (2004) 3–14, https://doi.org/10.1016/j.micromeso.2004.03.034.
[3] S. Zheng, Y. Sun, H. Xue, P. Braunstein, W. Huang, H. Pang, Dual-ligand and hard–soft acid–base strategies to optimize metal–organic framework nanocrystals for stable electrochemical cycling performance, Natl. Sci. Rev. 9 (7) (2022) nwab197, https://doi.org/10.1093/nsr/nwab197.
[4] P. Rajkumar, J.K. Ramesh, V. Thirumal, M.S. Iyer, R.M. Bhackiyavathi Princess, R. M. Gnanamuthu, K. Yoo, J. Kim, Unlocking the potential of a MOF-derived $CaMoO_4$ electrode for high-performance supercapacitor applications, New J. Chem. 48 (2024) 13238–13244, https://doi.org/10.1039/D4NJ02563F.
[5] M.S. Vaishali, N. Priyadarshini, P. Nagapandiselvi, C. Chandraleka, Calcium molybdate/activated carbon nanocomposite: A dual-functional material for energy storage and photocatalytic applications, Colloids Surf. A: Physicochem. Eng. Asp. 721 (2025) 137207, https://doi.org/10.1016/j.colsurfa.2025.137207.
[6] F. Ali, N.R. Khalid, G. Nabi, A. Ul-Hamid, M. Ikram, Hydrothermal synthesis of cerium-doped Co_3O_4 nanoflakes as an electrode for supercapacitor applications, Int. J. Energy Res. 45 (2021) 1999–2010, https://doi.org/10.1002/er.5893.
[7] W. Sun, K. Song, M. Zhu, et al., Effect of Ce content on the magnetic properties and microstructure of $CeCo_5$-based sintered bulk magnets, J. Supercond. Nov. Magn. 31 (2018) 1761–1765, https://doi.org/10.1007/s10948-017-4387-8.
[8] Y. Jin, W. Xiao, L. Ma, X. Liang, S. Ma, W. Sun, P. Zhang, J. Cui, D. Wang, Effect of Ce doping on electromagnetic characteristics and absorbing properties of M-type barium ferrite, Mater. Today Commun. 39 (2024) 108596, https://doi.org/10.1016/j.mtcomm.2024.108596.
[9] H.N. Abdelhamid, G.A. Mahmoud, W.A. Sharmouk, A cerium-based MOFzyme with multi-enzyme-like activity for the disruption and inhibition of fungal recolonization, J. Mater. Chem. B 8 (2020) 7548–7556, https://doi.org/10.1039/D0TB00894J.
[10] Y. Alajlani, W. Sharmoukh, Nanocrystalline Ce/Sb substituted ZnO compositions: Tailoring of room temperature ferromagnetism for spintronics technology, J. Magn. Magn. Mater. 621 (2025) 172937, https://doi.org/10.1016/j.jmmm.2025.172937.
[11] P. Rajkumar, V. Thirumal, A.S. Rasappan, M.S. Iyer, S. Asaithambi, K. Yoo, J. Kim, Electrochemically enhanced battery-type Ni-substituted CaMo-MOF electrodes: Towards futuristic energy storage systems, J. Energy Storage 80 (2024) 110284, https://doi.org/10.1016/j.est.2023.110284.
[12] Z. Hou, R. Chai, M. Zhang, C. Zhang, P. Chong, Z. Xu, G. Li, J. Lin, Fabrication and luminescence properties of one-dimensional $CaMoO_4$:Ln^{3+} (Ln = Eu, Tb, Dy) nanofibers via electrospinning process, Langmuir 25 (20) (2009) 12340–12348, https://doi.org/10.1021/la9016189.
[13] P.M. Usov, C. McDonnell-Worth, F. Zhou, D.R. MacFarlane, D.M. D'Alessandro, The electrochemical transformation of the zeolitic imidazolate framework ZIF-67 in aqueous electrolytes, Electrochim. Acta 153 (2015) 433–438, https://doi.org/10.1016/j.electacta.2014.11.150.
[14] T. Thongtem, A. Phuruangrat, S. Thongtem, Characterization of $MMoO_4$ (M = Ba, Sr and Ca) with different morphologies prepared using cyclic microwave radiation, Mater. Lett. 62 (3) (2008) 454–457, https://doi.org/10.1016/j.matlet.2007.05.059.
[15] W. Sharmoukh, Z.M. Hassan, S.G. Mohamed, H.N. Abdelhamid, Metal–organic frameworks (UiO-66-NH_2)/PEDOT-derived ZrO_2/N,S-doped carbon for supercapacitors, J. Energy Storage 102 (2024) 114071, https://doi.org/10.1016/j.est.2024.114071.
[16] H. Molavi, Cerium-based metal–organic frameworks: Synthesis, properties, and applications, Coord. Chem. Rev. 527 (2025) 216405, https://doi.org/10.1016/j.ccr.2024.216405.
[17] M. Zhang, Y. Li, X. Liu, C. Shen, Cerium-based materials in burn wound healing: Development, mechanism and outlook, Regenes. Repair Rehabil. 1 (3) (2025) 6–15, https://doi.org/10.1016/j.rerere.2025.01.001.
[18] E. Leysour de Rohello, Y. Suffren, F. Gouttefangeas, O. Merdrignac-Conanec, O. Guillou, F. Cheviré, Synthesis, luminescence and energy transfer properties of Ce^{3+}/Mn^{2+} co-doped calcium carbodiimide phosphors, Inorganics 11 (7) (2023) 291, https://doi.org/10.3390/inorganics11070291.
[19] M. Minakshi, D.R.G. Mitchell, C. Baur, J. Chable, A.J. Barlow, M. Fichtner, R. Ahuja, Phase evolution in calcium molybdate nanoparticles as a function of synthesis temperature and its electrochemical effect on energy storage, Nanoscale Adv. 1 (2) (2019) 565–580, https://doi.org/10.1039/C8NA00156A.
[20] H. Zhai, J. Qi, Y. Tan, L. Yang, H. Li, Y. Kang, H.S. Park, Construction of 1D-MoS_2 nanorods/$LiNb_3O_8$ heterostructure for enhanced hydrogen evolution, Appl. Mater. Today 18 (2020) 100536, https://doi.org/10.1016/j.apmt.2019.100536.
[21] R. Pitcheri, S.P. Mooni, D. Radhalayam, M. Nora, S. Roy, F.A.M. Al-Zahrani, M. Suneetha, Effect of Ce-doping on the structural, morphological and electrochemical features of Co_3O_4 nanoparticles synthesized by solution

combustion method for battery-type supercapacitors, Ceram. Int. 50 (23) (2024) 50504–50515, https://doi.org/10.1016/j.ceramint.2024.09.396.
[22] Y. Zhu, W. Du, Q. Zhang, H. Yang, Q. Zong, Q. Wang, Z. Zhou, J. Zhan, A metal–organic framework template-derived hierarchical Mo-doped LDHs@MOF-Se core–shell array electrode for supercapacitors, Chem. Commun. 56 (2020) 13848–13851, https://doi.org/10.1039/D0CC05561A.
[23] Q. Wang, X. Ran, W. Shao, M. Miao, D. Zhang, High-performance flexible supercapacitor based on metal–organic-framework-derived $CoSe_2$ nanosheets on carbon nanotube film, J. Power Sources 490 (2021) 229517, https://doi.org/10.1016/j.jpowsour.2021.229517.
[24] B. Ameri, A.M. Zardkhoshoui, S.S.H. Davarani, Metal–organic framework derived hollow manganese nickel selenide spheres confined with nanosheets on nickel foam for hybrid supercapacitors, Dalton Trans. 50 (2021) 8372–8384, https://doi.org/10.1039/D1DT01215K.
[25] S. Dai, Y. Yuan, J. Yu, J. Tang, J. Zhou, W. Tang, Metal–organic framework-templated synthesis of sulfur-doped core–sheath nanoarrays and nanoporous carbon for flexible all-solid-state asymmetric supercapacitors, Nanoscale 10 (2018) 15454–15461, https://doi.org/10.1039/C8NR03743D.
[26] A. Bahaa, J. Balamurugan, N.H. Kim, J.H. Lee, Metal–organic framework derived hierarchical copper cobalt sulfide nanosheet arrays for high-performance solid-state asymmetric supercapacitors, J. Mater. Chem. A 7 (2019) 8620–8632, https://doi.org/10.1039/C9TA00265K.
[27] D. Martínez-Díaz, P. Leo, D.M. Crespo, M. Sánchez, A. Ureña, Direct synthesis of MOF-74 materials on carbon fiber electrodes for structural supercapacitors, Nanomaterials 14 (2) (2024) 227, https://doi.org/10.3390/nano14020227.
[28] C.M. Hangarter, B. Dyatkin, M. Laskoski, M.C. Palenik, J.B. Miller, M. Tyagi, C. A. Klug, A cobalt-based layered MOF material for supercapacitor applications, J. Energy Storage 89 (2024) 111476, https://doi.org/10.1016/j.est.2024.111476.
[29] M. Ma, H. Li, H. Zhang, D. Pan, Solution-deposited highly luminescent Eu^{3+}-doped $CdMoO_4$ thin films, J. Lumin. 203 (2018) 702–706, https://doi.org/10.1016/j.jlumin.2018.07.023.